Computational Geosciences

Implementation and evaluation of permeability-porosity and tortuosity-porosity relationships linked to mineral dissolution-precipitation

--Manuscript Draft--

Manuscript Number:	
Full Title:	Implementation and evaluation of permeability-porosity and tortuosity-porosity relationships linked to mineral dissolution-precipitation
Article Type:	SI: Subsurface Environmental Simulation Benchmarks
Keywords:	Permeability-porosity relationship, tortuosity-porosity relationship, mineral dissolution-precipitation, benchmark, CrunchFlow, HP1, MIN3P, PFlotran, TOUGHREACT
Corresponding Author:	Mingliang Xie, Ph.D. The University of British Columbia Vancouver, British Columbia CANADA
Corresponding Author Secondary Information:	
Corresponding Author's Institution:	The University of British Columbia
Corresponding Author's Secondary Institution:	
First Author:	Mingliang Xie, Ph.D.
First Author Secondary Information:	
Order of Authors:	Mingliang Xie, Ph.D.
	K. Ulrich Mayer, Ph.D.
	Francis Claret, Ph.D.
	Peter Alt-Epping, Ph.D.
	Diederik Jacques
	Carl Steefel, Ph.D.
	Christophe Chiaberge
	Jiri Simunek, Ph.D.
Order of Authors Secondary Information:	

Abstract:	Changes of porosity, permeability and tortuosity due to physical and geochemical processes are of vital importance for a variety of hydrogeological systems, including passive treatment facilities for contaminated groundwater, Engineered Barrier Systems (EBS), and host rocks for high-level nuclear waste (HLW) repositories. Due to the non-linear nature and chemical complexity of the problem, it is impossible to verify reactive transport codes analytically, and code inter-comparisons are the most suitable method to assess code capabilities and model performance. This paper summarizes model inter-comparisons for six hypothetical scenarios with generally increasing geochemical or physical complexity using the reactive transport codes CrunchFlow, HP1, MIN3P, PFlotran, and TOUGHREACT. Benchmark problems include the enhancement of porosity and permeability through mineral dissolution, as well as near complete clogging due to localized mineral precipitation, leading to the reduction of permeability and tortuosity. Processes considered in the benchmark simulations are advective-dispersive transport in saturated media, kinetically controlled mineral dissolution-precipitation, and aqueous complexation. Porosity changes are induced by mineral dissolution-precipitation reactions and the Carman-Kozeny relationship is used to describe changes in permeability as a function of porosity. Archie's law is used to update the tortuosity and the pore diffusion coefficient as a function of porosity. Results demonstrate that, generally, good agreement is reached amongst the computer models despite significant differences in model formulations. Some differences are observed, in particular for the more complex scenarios involving clogging; however,

| | these differences do not affect the interpretation of system behavior and evolution. |

1   **Implementation and evaluation of permeability-porosity and tortuosity-**

2   **porosity relationships linked to mineral dissolution-precipitation**

3   Mingliang Xie[1,*], K. Ulrich Mayer[1], Francis Claret[2], Peter Alt-Epping[3], Diederik Jacques[4], Carl
4   Steefel[5], Christophe Chiaberge[2] and Jiri Simunek[6]
5
6
7
8   1. Department of Earth, Ocean and Atmospheric Sciences. The University of British Columbia,

9   Vancouver, BC, Canada

10 2. BRGM, 45060 Orleans Cedex, France

11 3. Rock-Water Interaction Group, University of Bern, Institute of Geological Sciences, 3012

12   Bern, Switzerland

13 4. Belgian Nuclear Research Centre SCK.CEN, Mol, Belgium B-2400

14 5. Lawrence Berkeley National Laboratory, Berkeley, CA 94720, USA

15 6. University of California, Riverside, CA 92521, USA

16 * Corresponding author mxie@eos.ubc.ca

Abstract

Changes of porosity, permeability and tortuosity due to physical and geochemical processes are of vital importance for a variety of hydrogeological systems, including passive treatment facilities for contaminated groundwater, Engineered Barrier Systems (EBS), and host rocks for high-level nuclear waste (HLW) repositories. Due to the non-linear nature and chemical complexity of the problem, it is impossible to verify reactive transport codes analytically, and code inter-comparisons are the most suitable method to assess code capabilities and model performance. This paper summarizes model inter-comparisons for six hypothetical scenarios with generally increasing geochemical or physical complexity using the reactive transport codes CrunchFlow, HP1, MIN3P, PFlotran, and TOUGHREACT. Benchmark problems include the enhancement of porosity and permeability through mineral dissolution, as well as near complete clogging due to localized mineral precipitation, leading to the reduction of permeability and tortuosity. Processes considered in the benchmark simulations are advective-dispersive transport in saturated media, kinetically controlled mineral dissolution-precipitation, and aqueous complexation. Porosity changes are induced by mineral dissolution-precipitation reactions and the Carman-Kozeny relationship is used to describe changes in permeability as a function of porosity. Archie's law is used to update the tortuosity and the pore diffusion coefficient as a function of porosity. Results demonstrate that, generally, good agreement is reached amongst the computer models despite significant differences in model formulations. Some differences are observed, in particular for the more complex scenarios involving clogging; however, these differences do not affect the interpretation of system behavior and evolution.

3

1   **Implementation and evaluation of permeability-porosity and tortuosity-**

2   **porosity relationships linked to mineral dissolution-precipitation**

3   Mingliang Xie[1,*], K. Ulrich Mayer[1], Francis Claret[2], Peter Alt-Epping[3], Diederik Jacques[4], Carl
4   Steefel[5], Christophe Chiaberge[2] and Jiri Simunek[6]
5
6
7
8   1. Department of Earth, Ocean and Atmospheric Sciences. The University of British Columbia,

9   Vancouver, BC, Canada

10 2. BRGM, 45060 Orleans Cedex, France

11 3. Rock-Water Interaction Group, University of Bern, Institute of Geological Sciences, 3012

12   Bern, Switzerland

13 4. Belgian Nuclear Research Centre SCK.CEN, Mol, Belgium B-2400

14 5. Lawrence Berkeley National Laboratory, Berkeley, CA 94720, USA

15 6. University of California, Riverside, CA 92521, USA

16 * Corresponding author mxie@eos.ubc.ca

1. Introduction

The simulation of permeability and tortuosity evolution due to porosity changes is of vital importance for the description of various hydrogeological processes, such as fluid circulation in geothermal systems (Wagner et al. 2005), acid rock drainage (ARD) attenuation and treatment (Annandale et al. 1999), well fouling due to oxide precipitation (Houben 2003), aquifer storage and recovery (ASR) (Rinck-Pfeiffer et al. 2000), and the long-term geochemical evolution of host rock considered for high-level nuclear waste (HLW) repositories (De Windt et al. 2004; Xie et al. 2011; Liu et al. 2014). Porosity changes can be the result of many processes including mechanical deformation, swelling of clay minerals (e.g. montmorillonite), dissolution/precipitation, and thermal deformation. Mineral dissolution and precipitation reactions can also have a significant effect on porous medium porosity and in turn permeability and tortuosity.

Porosity changes in natural porous media occur normally very slowly, but in the long term can be of pivotal importance for the migration of fluids and solutes. If porosity increases are substantial, preferential fluid migration pathways may develop, accelerating solute transport. On the other hand, for significant porosity decreases, nearly complete clogging may occur, substantially inhibiting fluid and solute migration. Clogging in particular is associated with numerical challenges due to the development of very small water-rock ratios, or the complete disappearance of the aqueous phase. It is therefore useful to evaluate the capabilities and performance of reactive transport codes to simulate evolving porosity and permeability, both for conditions of porosity enhancement and reduction. It is also of interest to evaluate the effect of changing tortuosity on pore diffusion, in particular for clogging-dominated problems. Considering the complex nature of reactive transport simulations, code verification through

40 analytical solutions is often impossible. Code inter-comparison through well-defined benchmarks

41 is in many cases the most suitable method (Carrayrou et al. 2010).

42 The present paper presents and analyses the results of an inter-comparison involving five

43 reactive transport codes (i.e. CrunchFlow, HP1, MIN3P, PFlotran, and TOUGHREACT) used

44 for the investigation of six hypothetical scenarios to evaluate formulations and implementations

45 for permeability-porosity and tortuosity-porosity relationships. Transport and reaction processes

46 considered include: multicomponent aqueous complexation, kinetic surface-controlled reversible

47 mineral dissolution and precipitation, advective and diffusive mass transport, and coupling of

48 dissolution-precipitation induced porosity change and fluid flow processes. The Carman-Kozeny

49 relationship was used to describe changes in permeability, and the tortuosity and pore diffusion

50 coefficients were updated based on Archie's law, both as a function of porosity.

2. Problem overview

52 Six benchmark levels with increasing complexity were investigated in this exercise (Table 1) –

53 the first level (B1) considers mineral dissolution and associated permeability enhancement, the

54 second level (B2) focuses on a precipitation-dominated (clogging) problem, and the third level

55 (B3) extends the clogging problem of benchmark B2 by considering a significantly more

56 complex geochemical system (e.g. inclusion of additional chemical components and minerals).

57 Benchmarks B1-B3 have in common that advection is the only transport process considered. The

58 fourth level (B4) is based on benchmark B3, but considers diffusive transport instead of

59 advective transport to compare the codes under purely diffusive mass transfer conditions. The

60 fifth level (B5) combines benchmarks B3 and B4, and includes both diffusive and advective

61 transport. Benchmarks B1-B5 were carried out for one-dimensional flow and transport systems

4

62 with initially homogeneous medium properties. Benchmark B6 further extends B5 into a 2D

63 heterogeneous problem with a randomly distributed conductivity field.

64   Benchmark B1 considers the infiltration of a sulfuric acid solution into a rock matrix

65 containing calcite in an otherwise non-reactive (inert) rock matrix. The only mineral phase

66 considered is calcite; four components are included (H^+, Ca^{2+}, CO_3^{2-}, and SO_4^{2-}), leading to the

67 formulation of 10 aqueous complexes. Benchmark B2 also considers the infiltration of a sulfuric

68 acid solution into a calcite-containing rock matrix. In addition to the primary mineral phase

69 calcite, gypsum is considered as a secondary phase. The inflow solution contains a much higher

70 SO_4^{2-} concentration. Benchmark B3 is based on B2 by adding Fe(II), Fe(III), K, Al, Na, and

71 $O_2(aq)$, thus increasing the number of aqueous components (10), secondary aqueous species (40)

72 and mineral phases (6). Benchmarks B4 to B6 use the same reaction network as Benchmark B3.

73 For Benchmarks B4 to B6, the chemical composition of the solution at the inflow boundary and

74 the pore water in the domain, and the mineral composition of the domain also remain the same as

75 those in Benchmark B3.

76   All simulations were conducted under standard pressure and temperature (25°C) and fully

77 saturated conditions. The geochemical database was derived from the database of MINTEQA2

78 (Allison et al. 1991, see Supporting Information).

79   This set of benchmarks was solved by five different reactive transport codes, namely:

80 CrunchFlow (Steefel et al. this issue; Steefel 2009), HP1 (Jacques et al. 2008a, b, restricted to

81 B1-B5, because it is a one-dimensional transport code), MIN3P (Mayer et al. 2002; Mayer 2010;

82 Mayer and MacQuarrie 2010), PFlotran (Lichtner et al. 2013), and TOUGHREACT (Xu et al.

83 2004, 2006, 2011). An overview on the formulations and capabilities of the individual codes is

84 given in Steefel et al. (this issue).

3. Theoretical background

The generalized governing equations for multicomponent reactive transport are provided in Steefel et al. (this issue) and are therefore not repeated here. This section focuses on the formulations used to describe permeability-porosity and tortuosity-porosity relationships, which are central to this benchmark. In addition, the formulations for mineral dissolution-precipitation reactions and activity corrections are provided, considering that these relationships strongly affect the results of the benchmarks.

3.1. Porosity, permeability, and tortuosity

The porosity change in each grid cell is calculated by summation over the volume fraction (φ) changes of the minerals that occurred between the new time step ($t+\Delta t$) and that at the previous time step (t). Assuming that porosity changes are occurring slowly, porosity (ϕ) in each cell is explicitly updated after completion of each time step:

$$\phi^{t+\Delta t} = \phi^t - \sum_{i=1}^{N_m} (\varphi_i^{t+\Delta t} - \varphi_i^{t}) \qquad (1)$$

where N_m defines the number of the minerals. The hydraulic conductivity K is also updated at the end of each time step according to the Carman-Kozeny relationship (Carrier, 2003):

$$K^{t+\Delta t} = \left[\frac{(\phi^{t+\Delta t})^3}{[1-(\phi^{t+\Delta t})]^2}\right]\left[\frac{(1-\phi^t)^2}{(\phi^t)^3}\right] K^t \qquad (2)$$

Archie's law is used to calculate the tortuosity τ as a function of porosity at the new time level:

$$\tau^{t+\Delta t} = [\phi^{t+\Delta t}]^\alpha \qquad (3)$$

with the exponent $\alpha = 1/3$, consistent with the formulation by Millington and Quirk (1961). The pore diffusion coefficient at the new time level ($D_p^{t+\Delta t}$) is calculated as:

6

$$D_p^{t+\Delta t} = \tau^{t+\Delta t} D_0 \qquad (4)$$

where D_0 is the free phase diffusion coefficient in water (assumed to be identical for all species).

The effective diffusion coefficient D_e is calculated as:

$$D_e^{t+\Delta t} = \phi^{t+\Delta t} \tau^{t+\Delta t} D_0 = \phi^{t+\Delta t} D_p^{t+\Delta t} \qquad (5)$$

3.2. Mineral dissolution-precipitation reactions

Mineral dissolution-precipitation reactions are described as kinetic surface-controlled reactions based on the rate expression:

$$R_i^m = -k_i^m \left[1 - \left(\frac{IAP_i^m}{K_i^m} \right) \right] \qquad (6)$$

where R_i^m is the reaction rate, IAP_i^m is the ion activity product, K_i^m is the equilibrium constant and k_i^m is the effective rate constant. The rate constants k_i^m of primary minerals vary as a function of mineral abundance at each time step. For primary mineral phases following a two-third power relationship of the form

$$k_i^{m,t} = -k_i^{m,0} \left(\frac{\varphi_i^t}{\varphi_i^0} \right)^{2/3} \qquad (7)$$

is used to update the effective rate constant (Lichtner, 1996). In this relationship, $k_i^{m,t}$ and φ_i^t define the effective rate constant and mineral volume fraction at time t, respectively; while $k_i^{m,0}$ and φ_i^0 define the initial rate constant and mineral volume fraction, respectively. The rate coefficients for secondary minerals are assumed to remain constant.

3.3. Activity corrections

Activity coefficients γ_i^d for all charged dissolved species A_i^d, where A_i^d can be either a component as species in solution or an aqueous complex, are calculated based on the modified

7

118 Debye-Hückel equation if ion-specific parameters are available (Parkurst 1990; Allison et al.

119 1991):

$$log\gamma_i^d = \frac{-A_d Z_i^2 \sqrt{I}}{1 + B_d a_i \sqrt{I}} + b_i I \qquad (8)$$

120 where I is the ionic strength, Z_i is the charge of the ith ion, A_d and B_d are constants, a_i and b_i are

121 ion-specific parameters. If a_i is available, but not b_i, equation (8) is used with $b_i = 0$. When a_i

122 is not provided, the Davies equation is used as an approximation (Allison et al. 1991):

$$log\gamma_i^d = -A_d Z_i^2 \left[\frac{\sqrt{I}}{1 + \sqrt{I}} - 0.24I \right] \qquad (9)$$

123 Activity correction for neutral species excluding water is calculated as described by Allison et al.

124 (1991):

$$log\gamma_i^d = 0.1I \qquad (10)$$

125 The activity correction for water is defined by (Allison et al. 1991):

$$\gamma_{H_2O} = 1 - 0.017 \sum_{i=1}^{N_d} C_i^d \qquad (11)$$

126 where C_i^d are the concentrations of the dissolved charged species and N_d defines the number of

127 the dissolved charged species (Allison et al. 1991).

3.4. **Numerical considerations**

129 Benchmark levels B1-B3 do neither consider diffusion, nor dispersion, in order to allow for a

130 better evaluation of numerical dispersion and operator-splitting errors as a function of different

131 model formulations. Because significant spatial differences develop for porosity, hydraulic

132 conductivity, and tortuosity, the spatial weighting of these parameters is important. Harmonic

133 averaging of all flow and transport parameters (i.e. hydraulic conductivity and tortuosity) were

134 adopted as the recommended default option for the simulations. For spatial weighting of the

135 advection terms, upstream weighting was used; implicit time weighting was used for time

136 integration.

4. Benchmark definition

4.1. Dimensions and spatial discretization

139 The 2m long 1D-domain for benchmarks B1 – B5 was discretized using a discretization interval

140 of $\Delta x = 0.025$ m, corresponding to 80 cells for uniform discretization, or 81 cells with half cells

141 on the boundaries. The 2D-domain (3 m in length and 2 m in height) for benchmark B6 was

142 discretized into 31x41=1271 cells (Figure 1).

4.2. Physical properties

144 For the 1D problems B1 to B5, the porous medium is initially homogeneous with an initial

145 porosity of 0.35 and an initial hydraulic conductivity of 1.16×10^{-4} m s^{-1} (10 m day^{-1}). An average

146 free phase diffusion coefficient of 1.0×10^{-9} m^{-2} s^{-1} for all aqueous species is considered for

147 benchmarks B4-B6. For problems including advection, dispersion is neglected to minimize the

148 complexity of the problem and facilitate a focused comparison of the different codes. In addition,

149 dispersion becomes insignificant when clogging occurs, due to reduced flow velocities and the

150 localized nature of pore clogging due to mineral precipitation. For the 2D problem B6, advective

151 and diffusive transport is considered in a similar fashion to B5. However, the porous medium is

152 characterized by a heterogeneous initial hydraulic conductivity field (Figure 1).

4.3. **Boundary conditions for flow**

Benchmarks B1-B4 considered constant hydraulic heads at the inflow (0.007 m) and outflow (0.0 m) boundaries. For Benchmark B4, no-flow conditions are enforced by setting equal hydraulic heads at the inflow and outflow boundaries. For benchmark B6, the hydraulic head at the inflow boundary was set at 0.0105 m to maintain the same hydraulic gradient as with all other benchmarks (except B4).

4.4. **Mineralogical and chemical parameters**

4.4.1. **Aqueous components and speciation reactions**

The components for benchmarks B1 and B2 are H^+, CO_3^{2-}, Ca^{2+}, SO_4^{2-} and Na^+. An enhanced set of components is used for benchmarks B3 – B6 (H^+, CO_3^{2-}, Ca^{2+}, SO_4^{2-} , Fe^{3+} , Fe^{2+}, Al^{3+} , K^+ , O_2(aq) and Na^+). Relevant aqueous complexation reactions and activity model parameters are tabulated in the Supporting Information.

4.4.2. **Minerals**

Mineral phases and their parameters are listed in Table 2 and Table 3. Benchmarks B1 and B2 use a subset of these mineral phases. All minerals are treated as kinetic surface-controlled dissolution/precipitation reactions. The only exception is jarosite, which was treated as an equilibrium reaction by HP1 owing to numerical difficulties. The initial rate constants ($k_i^{m,0}$) are shown in Table 3.

4.4.3. **Initial and boundary conditions for reactive transport**

Benchmark B1: The only mineral phase considered is calcite at a volume fraction of 0.30 m^3 m^- ^{3}, the remaining fraction of the solid phase is assumed inert. The solution domain is initially

10

174   occupied by an alkaline solution in equilibrium with calcite. The infiltrating water is acidic with

175   a pH of 3 and is undersaturated with respect to calcite (Table 4). A third type boundary condition

176   (specified mass flux) is used at the inflow boundary and a free exit boundary is used at the

177   outflow.

178   **Benchmark B2:** The mineral phases considered in the system are calcite and gypsum. The

179   domain initially includes only calcite with a volume fraction of 0.30 m^3 m^{-3} (Table 5). Resident

180   pore water is in equilibrium with calcite and undersaturated with respect to gypsum (Table 6).

181   With the infiltration of a sulfuric acid solution (pH = 3) containing CO_3^{2-}, Ca^{2+}, SO_4^{2-} and Na^+,

182   calcite dissolves and gypsum precipitates, followed by gypsum re-dissolution near the inflow

183   boundary. The initial and boundary geochemical compositions for the aqueous phases are listed

184   in Table 6. Boundary conditions are set as in B1.

185   **Benchmarks B3 – B6:** The domain initially contains calcite with a volume fraction of 0.22 m^3

186   m^{-3}), as well as gibbsite (0.05 m^3 m^{-3}) and siderite (0.05 m^3 m^{-3}) (Table 7). The initial and

187   boundary total component concentrations in the aqueous phases are listed in Table 8. The

188   incoming solution is acidic and undersaturated with respect to all minerals, except jarosite. This

189   boundary condition was specified to induce jarosite precipitation near the inflow. The

190   background solution is slightly alkaline and is in equilibrium with calcite, siderite, gibbsite, and

191   ferrihydrite. The initial volume fraction of calcite (0.22 m^3 m^{-3}) is lower than that in B2. The

192   lower calcite content limits secondary gypsum formation, which is offset by additional

193   precipitation of ferrihydrite, siderite, gibbsite and jarosite. This approach is taken to provide a

194   suitable benchmark that evaluates system evolution under near clogging conditions. Boundary

195   conditions are set as in B1 and B2, with the exception of Benchmark B4 which uses first type

196   (Dirichlet) boundary conditions at the inflow and outflow ends of the column.

5. Results

Simulated results by all codes are discussed in the following subsections. Reference model results produced by MIN3P are also provided in tabular format in the Supporting Information.

5.1. **B1 – Porosity & permeability change due to dissolution**

Simulation results for benchmark B1 show the gradual dissolution of calcite along an initially narrow dissolution front, which widens as permeability and flow velocities increase (Figure 2). Although porosity and permeability increase substantially near the inflow end already at early time, total flow rate increases are relatively moderate during the first 100 years. However, a rapid increase in flow rate is predicted, once calcite depletion approaches the outflow end of the simulation domain. All profiles of porosity, permeability and hydraulic head at 10 and 100 years calculated by the five codes are nearly identical, demonstrating very good agreement between the models, despite different transport schemes and coupling methods. Slight differences exist for results at 120 years. This time correlates with the breakthrough of the dissolution front and is naturally most sensitive to deviations. The time curves of the flux at the outflow boundary are identical for all codes up to 120 years.

5.2. **B2 – Clogging due to dissolution/precipitation (simple reaction network)**

Simulation results show that the intrusion of the sulfuric acid solution causes the dissolution of calcite and formation of gypsum (Figure 3). Although gypsum re-dissolves near the inflow, a narrow region of gypsum accumulation causes clogging of the flow path. The zone of gypsum accumulation is already visible after 10 years; however, significant porosity remains at this time. After 100 years, clogging is nearly complete and flow rates are greatly reduced, resulting in negligible clogging front migration over the remaining 900 years. Simulated results show good

219   agreement between all codes. The maximum volume fraction of gypsum reaches 62.6% and

220   results in the reduction of porosity with a minimum value of 0.0016 after 1000 years at x=0.425

221   m (MIN3P, PFlotran and TOUGHREACT), at x=0.40 m with a minimum porosity of 0.003

222   (HP1) and at x=0.40 m with a minimum porosity of 0.0018 (CrunchFlow). The simulated

223   profiles of the hydraulic head show a sharp decline at the clogging point. The calculated flux at

224   the outflow boundary decreased rapidly within the first 100 years and more gradually after 500

225   years (Figure 3), showing good agreement amongst all codes with small deviations by HP1

226   owing to the higher minimum value of porosity by HP1.

227   ## 5.3.   **B3 – Clogging due to dissolution/precipitation (complex reaction**

228   **network - advection)**

229   Simulated results (Figure 4 and Figure 5) show that with the infiltration of the acidic solution,

230   calcite dissolves, while other minerals like gypsum, siderite, gibbsite, ferrihydrite dissolve or

231   precipitate depending on the time and location, thus forming various porosity modifications

232   along the flow path at different time levels (Figure 5). Jarosite precipitates near the inflow,

233   consequently, the porosity decreases near the infiltration boundary. However, the major porosity

234   reduction occurs due to the dissolution of calcite and precipitation of gypsum, similar to

235   benchmark level B2. At 10 years, the minimum porosity reduces from the initial value of 0.35 to

236   0.05 at 0.25 m, showing a tendency for clogging (Figure 4). The "clogging point" develops and

237   moves further downstream to 0.45 m at 100 years. Beyond 100 years, however, the clogging

238   point moves more slowly (Figure 4 top left), as clogging is nearly complete and water and solute

239   fluxes are greatly reduced. At 300 years, the minimum porosity reached is 0.0044 (CrunchFlow),

240   0.0020 (HP1), 0.0028 (MIN3P), 0.0022 (PFlotran) and 0.0048 (TOUGHREACT).

241   Overall, the model results compare well for all five codes; all models are in good

242   agreement with respect to the prediction of the mineral distribution and clogging location.

243   However, there appears to be significant differences in terms of outflux at the end of the

244   simulation (ranging over approximately 2 orders of magnitude). On the other hand, this apparent

245   mismatch has to be put into perspective. Comparing the residual outflux to the initial outflux at T

246   = 0 demonstrates that all models predict a reduction of flux by greater than 99.9%, which again

247   points to a very good agreement in terms of predicting both hydrogeologic and geochemical

248   evolution. Reasons for residual differences are likely due to the high sensitivity of fluxes to

249   minor variations in porosity, which in turn is affected by the formation and dissolution of

250   multiple mineral phases. These results highlight the challenges that numerical models encounter

251   due to clogging and phase disappearance.

252   5.4. **B4 – Clogging due to dissolution/precipitation (complex reactions**
253   **network - diffusion)**

254   Diffusive transport results in a similar geochemical evolution as simulated in the advective case

255   (B3), but with mineral dissolution/precipitation fronts that are moving more slowly.

256   Consequently, the kinetic limitations have a smaller effect on the results, which can be seen by

257   the comparison of the profiles for jarosite. Jarosite was treated as a kinetically controlled mineral

258   dissolution/precipitation reaction by all codes except HP1. The simulated results at 100 and

259   1000 years by HP1 agree better to those by CrunchFlow, MIN3P and PFlotran in comparison to

260   Benchmark B3 (compare Figure 7 and Figure 5). Figure 6 (left) shows a region of reduced

261   porosity, leading to reductions in tortuosity and effective diffusion coefficients (D_e) (Figure 6

262   right). The point with minimal porosity is located at 0.325 m after 3000 years. Simulated

263   geochemical and hydrogeological evolution (Figure 6) as well as mineralogical composition

14

264 (Figure 7) by all participating codes showed good agreement. Generally, the simulated profiles

265 of mineral volume fractions by MIN3P, CrunchFlow and PFlotran agree very well with slight

266 difference for ferrihydrite and jarosite. Simulated mineral composition profiles by

267 TOUGHREACT and HP1 showed slightly faster moving fronts for all minerals, but visual

268 agreement among all codes can be considered as good.

269 ## 5.5. **B5 – Clogging due to dissolution/precipitation (complex chemical**

270 **reactions – advection and diffusion)**

271 Overall, the predicted geochemical and hydrogeological evolution (Figure 8), as well as

272 mineralogical composition (Figure 9) are in agreement for all participating codes. The clogging

273 positions of all simulations are at 0.5 m, which closely coincides with the position determined in

274 Benchmark B3. This indicates that the clogging position is controlled by the advective mass

275 transport for the benchmark set considered here. The distributions of most minerals in B4

276 resemble those of B3 with slight differences in the location of the moving fronts except jarosite

277 simulated by HP1. This can be explained because jarosite precipitation is treated as an

278 equilibrium phase instead of kinetic precipitation, as specified in the benchmark.

279 In contrast to Benchmark B3, larger differences can be seen for outflux and minimum

280 porosity (Figure 8). The simulated fluxes are fairly close within the first 90 years. At later time,

281 simulated fluxes by MIN3P, HP1, PFlotran and CrunchFlow decrease gradually (Figure 8), while

282 TOUGHREACT results suggest a substantial reduction of permeability that remains constant

283 after about 160 years. Although all fluxes are small in relation to the initial flux through the

284 system, the final predicted outfluxes vary by more than four orders of magnitude. The predicted

285 outfluxes by MIN3P, PFlotran and CrunchFlow vary by less than two orders of magnitude.

286 These differences suggest that the numerical formulation of diffusion processes plays a key role

287   for simulating porosity evolution, despite the fact that the problem is initially advection-

288   dominated. In comparison to B3, reduction of fluxes occurs smoothly (compare Figure 4 and

289   Figure 8). This indicates that diffusion tends to slow down clogging in this scenario but leads to

290   substantial reduction of the minimum porosity and flux in the long term.

291   ### 5.6. **B6 – Clogging due to dissolution/precipitation in heterogeneous media**

292   Simulated porosities for the 2D heterogeneous scenario are depicted in Figure 10 for two

293   selected observation points P1 (x = 0.1 m, z = 1.0 m) and P2 (x = 0.5 m, z = 1.0 m) for MIN3P,

294   CrunchFlow, TOUGHREACT and PFlotran. At P2 all simulated results of porosity evolution

295   show good agreement – with a rapid decrease during the first 20 years and a slight increase

296   thereafter (Figure 10). At P1, the simulated porosity show the same trend for the first 10 years,

297   but the minimum porosity values differ substantially. At later time, the porosity increases again,

298   gently according to MIN3P and CrunchFlow results, but more strongly according to the results

299   obtained with PFlotran and TOUGHREACT.

300   The simulated flux curves by MIN3P, CrunchFlow, TOUGHREACT and PFlotran show

301   a gradually decreasing trend with good agreement (Figure 11). The flux declined very rapidly

302   over the first 10 years, during which all simulated results are almost identical. At later times, the

303   flux continues to decrease but at a reduced rate. These results seem to contradict the simulated

304   porosity evolution at the observation points, which showed substantial differences at P1.

305   However, these results also indicate that the overall permeability evolution is reproduced in a

306   similar fashion by all codes, and that differences are local.

307   This observation is confirmed further by examining simulated 2D porosity distributions at

308   300 years. Results obtained with the different codes showed very similar pattern illustrating the

309   effect of heterogeneity on clogging (Figure 12). The low porosity zones (in blue), distributed

310 between x = 0.4 and 0.7 m, tend to form a continuous low permeability belt, which prevents flow

311 through the domain. The high porosity zones (in red) formed through the dissolution of calcite

312 and are most prevalent in the regions of higher initial hydraulic conductivity (compare Figure 12

313 and Figure 1).

6. Discussion

315 We acknowledge that the Carman-Kozeny relationship and Archie's law are not the only

316 relationships to describe the dependency of permeability and tortuosity on porosity. Multiple

317 alternative relationships exist to describe permeability and tortuosity evolution (e.g. Saripalli et

318 al. 2001). The model comparison presented here showed good agreement between the five codes,

319 but this does not imply that any of the codes – as is – is applicable to simulate permeability or

320 tortuosity evolution at a field site or in a laboratory experiment. It needs to be evaluated whether

321 the implemented relationships are suitable for the site or experimental conditions. However,

322 most of the alternative relationships such as for example the Brinkmann or Fair-Hatch models for

323 permeability will also be a function of porosity (Le Gallo et al. 1998) and the general findings of

324 the present investigation should therefore also be relevant for other approaches. Lastly, it has to

325 be recognized that permeability and tortuosity are not only functions of porosity, but may also

326 depend on micro-structural transformations that are taking place, i.e. different secondary

327 minerals may affect permeability in different ways due to their different growth habit (Gouze and

328 Coudrain-Ribstein, 2002).

7. Conclusions

330 A six-level benchmark problem with increasing complexity for flow, geochemical and

331 mineralogical conditions was analysed with five different reactive transport codes (i.e.

17

332   CrunchFlow, HP1, MIN3P, PFlotran and TOUGHREACT). The purpose of the benchmarking

333   exercise was to evaluate the robustness of various numerical implementations of permeability-

334   porosity and tortuosity-porosity relationships to assess the feedback between flow and reactive

335   transport with the potential for local phase disappearance, and the tendency for complete

336   clogging due to mineral precipitation.

337   Generally speaking, the simulation results appear to be robust and not dependent on the

338   employed code. Simulating porosity enhancement due to mineral dissolution proved to be an

339   easier task than simulating clogging. Increasing complexity due to the inclusion of additional

340   transport mechanisms and a more complex mineralogical assemblage had an impact on the

341   agreement of the model results obtained by the various codes. Although all codes showed good

342   agreement of the predicted mineralogical assemblage and the clogging locations, absolute values

343   of mass fluxes differed substantially. As discussed, these results have to be seen in perspective,

344   considering that the results of all codes agree in the sense that flux reductions are near 100% for

345   the clogging scenarios. Although differences exist in terms of the absolute flux values, the

346   impact on interpretation of the results would be very limited or even negligible. Nevertheless,

347   these results highlight the difficulties to simulate problems with pore clogging and phase

348   disappearance. Interestingly, the 2D problem (B6) showed better agreement among the codes

349   than the equivalent 1D problem (B5), despite the additional complexity in terms of

350   dimensionality and heterogeneity. Although local differences in porosity and mineral assemblage

351   were significant, agreement between overall outflow was good.

352   This benchmarking exercise also highlights that the implementation of the permeability-

353   porosity and tortuosity-porosity relationships, the activity correction model, and the numerical

354   methods (e.g. spatial weighting schemes) can significantly affect the benchmarking results. A

355   consistent numerical treatment is crucial for the benchmarking of reactive transport codes.

356

357   **Acknowledgements:**

362 **References:**

363 Allison, J.D., D.S. Brown, and K.J. Novo-Gradac (1991). MINTEQA2/PRODEFA2, A

364   Geochemical Assessment Model for Environmental Systems: Version 3.0 User's

365   Manual. United States Environmental Protection Agency, Office of Research and

366   Development, Washington, DC, EPA/600/3-91/021, 106p. [MTQ3.11]

367 Annandale, J.G., Jovanovic, N.Z., Benadè, N. and Tanner, P.D. (1999). Modelling the long-

368   term effect of irrigation with gypsiferous water on soil and water resources,

369   Agriculture, Ecosystems and Environment 76, 109–119.

370 Carrayrou, J., Hoffmann, J., Knabner, P., Kräutle, S., de Dieuleveult, C., Erhel, J., van der

371   Lee, J., Lagneau, V., Mayer, K. U., Macquarrie, K. T. B. (2010). Comparison of

372   numerical methods for simulating strongly nonlinear and heterogeneous reactive

373   transport problems-the MoMaS benchmark case. Computational Geosciences, 14 (3),

374   483 – 502

375 Carrier, W. D. (2003). Goodbye, Hazen; Hello, Kozeny-Carman, Journal of Geotechnical and

376   Geoenvironmental Engineering, 129(11), 1054-1056. doi:10.1061/(ASCE)1090-

377   0241(2003)129:11(1054).

378 De Windt, L., Pellegrini, D. and van der Lee, J. (2004). Coupled modeling of

379   cement/claystone interactions and radionuclide migration, J. Contaminant Hydrology,

380   68(3-4) 165-182.

381 Gouze, P., Coudrain-Ribstein, A., (2002). Chemical reactions and porosity changes during

382   sedimentary diagenesis. Appl. Geochem. 17, 39–47.

383 Houben, G.J., (2003).Corrigendum to iron oxide incrustations in wells—Part 1: Genesis,

384   mineralogy and geochemistry, Applied Geochemistry 18 (6): 927–939.

385 Jacques, D., J. Šimůnek, D. Mallants, and M. Th. van Genuchten, (2008a). Modelling

386   coupled hydrogeological and chemical processes in the vadose zone: a case study of

387   long-term uranium transport following mineral P-fertilization, Vadose Zone Journal,

388   7(2), 698-711.

389 Jacques, D., J. Šimůnek, D. Mallants and M. Th. van Genuchten, (2008b). Modelling coupled

390   water flow, solute transport and geochemical reactions affection heavy metal migration

391   in a Podzol soil, Geoderma, 145, 449-461, 2008b.

392 Le Gallo, Y., Bildstein, O., Brosse, E., (1998). Coupled reaction-flow modelling of

393   diagenetic changes in reservoir permeability, porosity and mineral compositions. J.

394   Hydrol. 209, 366–388.

395 Lichtner, P.C. (1996). In: Lichtner, P.C., Steefel, C.I., Oelkers, E.H. (Eds.). Continuum

396   Formulation of Multicomponent-Multiphase Reactive Transport, Vol. 34.

397   Mineralogical Society of America. Washington, DC, pp. 1–81 (Chapter 1).

398 Lichtner, P.C., G.E. Hammond. C. Lu, S. Karra, G. Bisht, B. Andre, R.T. Mills, J. Kumar

399   (2013) PFLOTRAN User manual: A Massively Parallel Reactive Flow and Transport

400   Model for Describing Surface and Subsurface Processes.

401 Liu, S., Jacques, D., Govaerts, J. and Wang, L., Conceptual model analysis of interaction at a

402   concrete–Boom Clay interface, Physics and Chemistry of the Earth,

403   http://dx.doi.org/10.1016/j.pce.2013.11.009 (in press).

404 Mayer, K.U., Frind, E.O., Blowes, D.W., (2002). Multicomponent reactive transport

405   modeling in variably saturated porous media using a generalized formulation for

406   kinetically controlled reactions. Water Resour. Res., 38: 1174.

407   Doi:10:1029/2001WR000862

408 Mayer, K.U., (2010). MIN3P User Guide, University of British Columbia, Department of
409   Earth and Ocean Sciences, March 27, 2010 (unpublished).

410 Mayer, K. U., and K. T. B. MacQuarrie, (2010). Solution of the MoMaS reactive transport
411   benchmark with MIN3P − Model formulation and simulation results, Comput. Geosci.,
412   14:405-419, doi:10.1007/s10596-009-9158-6

413 Millington, R. J., Quirk, J. P. (1961). Permeability of porous solids, Trans. Faraday Soc., 57,
414   1200–1207.

415 Parkhurst, D. L. and Appelo, C. A. J., (1999). User's guide to phreeqc − a computer program
416   for speciation, batch-reaction, one-dimensional transport, and inverse geochemical
417   calculations. In: Survey, U. S. G. (Ed.), Water-resources investigations, Denver
418   (Colorado).

419 Rinck-Pfeiffer SM, Ragusa SR, Sztajnbok P, Vandevelde T. (2000). Interrelationships
420   between biological, chemical and physical processes as an analog to clogging in aquifer
421   storage and recovery (ASR) wells. Water Research. 34(7): 2110–2118.

422 Saripalli, K.P., Meyer, P.D., Bacon, D.H., Freedman, V.L., (2001). Changes in hydrologic
423   properties of aquifer media due to chemical reactions: a review. Crit. Rev. Environ.
424   Sci. Technol. 31(2): 311-349.

425 Steefel, C. I., (2009). CrunchFlow user's manual. Software for modeling multicomponent
426   reactive flow and transport. Lawrence Berkeley National Laboratory.

427 Wagner, R., Kühn, M. , Meyn, V., Pape, H., Vath, U. and Clauser, C. (2005). Numerical
428   simulation of pore space clogging in geothermal reservoirs by precipitation of
429   anhydrite, International Journal of Rock Mechanics & Mining Sciences 42, 1070–1081.

430 Xie, M., Kolditz, O. and Moog, H.C. (2011). A geochemical transport model for thermo-

431 hydro-chemical (THC) coupled processes with saline water, Water Resources Research,

432 47(2), W02545, DOI: 10.1029/2010WR009270.

433 Xu, T., Sonnenthal, E. L., Spycher, N., and Pruess, K., (2004). TOUGHREACT user's guide:

434 A simulation program for non-isothermal multiphase reactive geochemical transport in

435 variable saturated geologic media. In: Lawrence Berkeley National Laboratory Report

436 LBNL-55460 (Ed.).

437 Xu, T., Sonnenthal, E., Spycher, N., and Pruess, K., (2006). TOUGHREACT—A simulation

438 program for non-isothermal multiphase reactive geochemical transport in variably

439 saturated geologic media: Applications to geothermal injectivity and CO_2 geological

440 sequestration. Computers & Geosciences 32, 145-165.

441 Xu, T., Spycher, N., Sonnenthal, E., Zhang, G., Zheng, L., and Pruess, K., (2011).

442 TOUGHREACT Version 2.0: A simulator for subsurface reactive transport under non-

443 isothermal multiphase flow conditions. Computers & Geosciences 37, 763-774.

444

Tables :

Table 1   **Overview of the benchmarks**

Benchmark Level	Description	Dimension	Processes	t_{Final}# [years]
B1	Dissolution only	1D homogeneous (2m in length)	advection, kinetic dissolution	500
B2	Clogging in a simple geochemical system		advection, kinetic dissolution/ precipitation	1000
B3	Clogging in a complex geochemical system		advection, kinetic dissolution/ precipitation, redox reactions	300
B4			Diffusion, no advection, kinetic dissolution/precipitation, redox reactions	3000
B5			advection, diffusion, kinetic dissolution/precipitation, redox reactions	300
B6		2D heterogeneous (3m in length and 2m in height)	advection, diffusion, kinetic dissolution/ precipitation, redox reactions	300

#- Final simulation time

Table 2   **Reaction stoichiometries and solubility constants for minerals**

Mineral	Reaction	$logK_{25}$
Calcite	$Ca^{2+} + CO_3^{2-} \leftrightarrow CaCO_3$	8.4750
Gypsum	$Ca^{2+} + SO_4^{2-} + 2H_2O \leftrightarrow CaSO_4{:}2H_2O$	4.5800
Ferrihydrite	$Fe^{3+} + 3H_2O \leftrightarrow Fe(OH)_3 + 3H^+$	-4.8910
Jarosite	$K^+ + 3Fe^{3+} + 2SO_4^{2-} + 6H_2O \leftrightarrow KFe_3(SO_4)_2(OH)_6 + 6H^+$	9.2100
Gibbsite	$Al^{3+} + 3H_2O \leftrightarrow Al(OH)_3 + 3H^+$	-8.1100
Siderite	$Fe^{2+} + CO_3^{2-} \leftrightarrow FeCO_3$	10.4500

Table 3   **Physical and kinetic mineral parameters**

Mineral	$k_i^{m,0}$ [m^2 mineral L^{-1} bulk]	Density [g cm^{-3}]	Mol. weight [g mol^{-1}]	Molar volume [cm^3 mol^{-1}]	Update type
Calcite	5×10^{-8}	2.71	100.09	36.93	twothird
Gypsum	5×10^{-8}	2.32	172.17	74.21	constant
Ferrihydrite	5×10^{-9}	4.37	104.87	23.99	constant
Jarosite	5×10^{-9}	3.20	494.81	154.63	constant
Gibbsite	5×10^{-10}	2.35	78.00	33.19	twothird
Siderite	5×10^{-9}	3.96	115.86	29.26	twothird

24

452

Table 4   Initial and boundary geochemical compositions in aqueous phase (B1)

Primary components	Unit	Initial condition	Boundary condition
pH	-	9.38	3.0
Ca^{2+}	mol l^{-1} H$_2$O	1.57×10^{-4}	1.00×10^{-4}
CO_3^{2-}	mol l^{-1} H$_2$O	2.57×10^{-4}	1.0×10^{-2}
SO_4^{2-}	mol l^{-1} H$_2$O	1.00×10^{-10}	6.46×10^{-4}

454

Table 5   Initial mineral composition and saturation index (SI) in the initial and boundary solutions (B2)

Mineral	Initial volume fraction [m^3 m^{-3}]	SI (IC solution)	SI (BC solution)
Calcite	0.3	0.0	-9.1
Gypsum	0.0	-3.1	-1.9

457

Table 6   Initial and boundary geochemical compositions in aqueous phase (B2)

Primary components	Unit	Initial condition (IC)	Boundary condition (BC)
pH	pH	9.33	3.0
Ca^{2+}	mol l^{-1} H$_2$O	1.70×10^{-4}	1.0×10^{-4}
CO_3^{2-}	mol l^{-1} H$_2$O	2.70×10^{-4}	1.0×10^{-2}
SO_4^{2-}	mol l^{-1} H$_2$O	1.70×10^{-4}	0.2
Na^+	mol l^{-1} H$_2$O	3.20×10^{-4}	3.96×10^{-1}

459

Table 7   Initial mineral composition and saturation index (SI) in the initial and boundary solutions (B3-B6)

Mineral	Initial volume fraction [m^3 m^{-3}]	SI (IC solution)	SI (BC solution)
Calcite	0.22	0.00	-8.93
Gypsum	0.00	-2.78	-2.02
Ferrihydrite	0.00	0.00	-0.07
Jarosite	0.00	-12.97	6.66
Gibbsite	0.05	0.00	-2.94
Siderite	0.05	0.00	-10.89

462

463 **Table 8** **Initial and boundary geochemical compositions in aqueous phase (B3-B6)**

Primary components	Unit	Initial condition (IC)	Boundary condition (BC)
pH	-	8.01	3.0
pe	-	-0.67	17.53
Ca^{2+}	mol l^{-1} H$_2$O	4.71×10^{-4}	1.00×10^{-4}
CO_3^{2-}	mol l^{-1} H$_2$O	2.19×10^{-3}	1.00×10^{-2}
SO_4^{2-}	mol l^{-1} H$_2$O	1.70×10^{-4}	1.00×10^{-1}
Na^+	mol l^{-1} H$_2$O	1.54×10^{-3}	9.09×10^{-2}
Al^{3+}	mol l^{-1} H$_2$O	2.81×10^{-7}	1.43×10^{-2}
K^+	mol l^{-1} H$_2$O	1.00×10^{-5}	7.67×10^{-5}
Fe^{2+}	mol l^{-1} H$_2$O	6.59×10^{-6}	1.14×10^{-8}
Fe^{3+}	mol l^{-1} H$_2$O	2.53×10^{-8}	2.23×10^{-2}

464
465
466
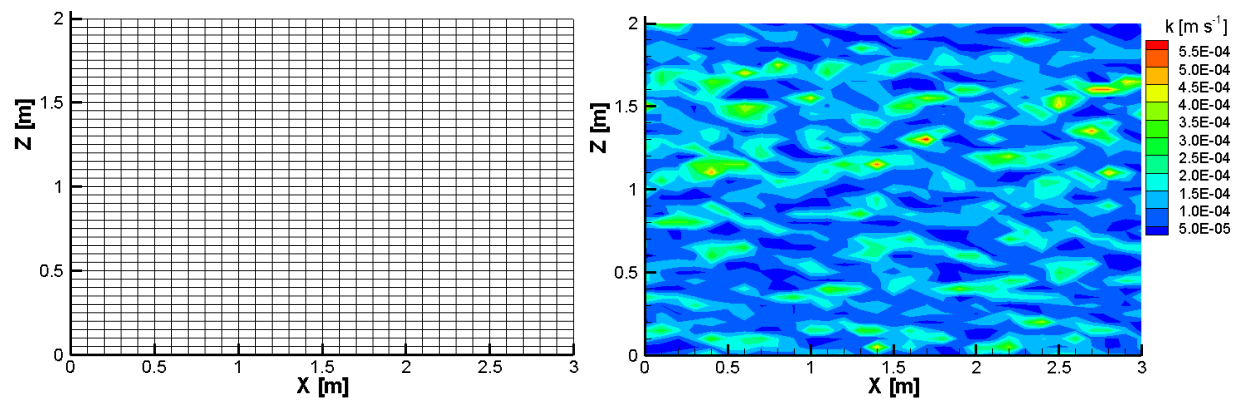467

Figures

Figure 1 **2D geometry (left) and initial hydraulic conductivity distribution (in [m s^{-1}])**
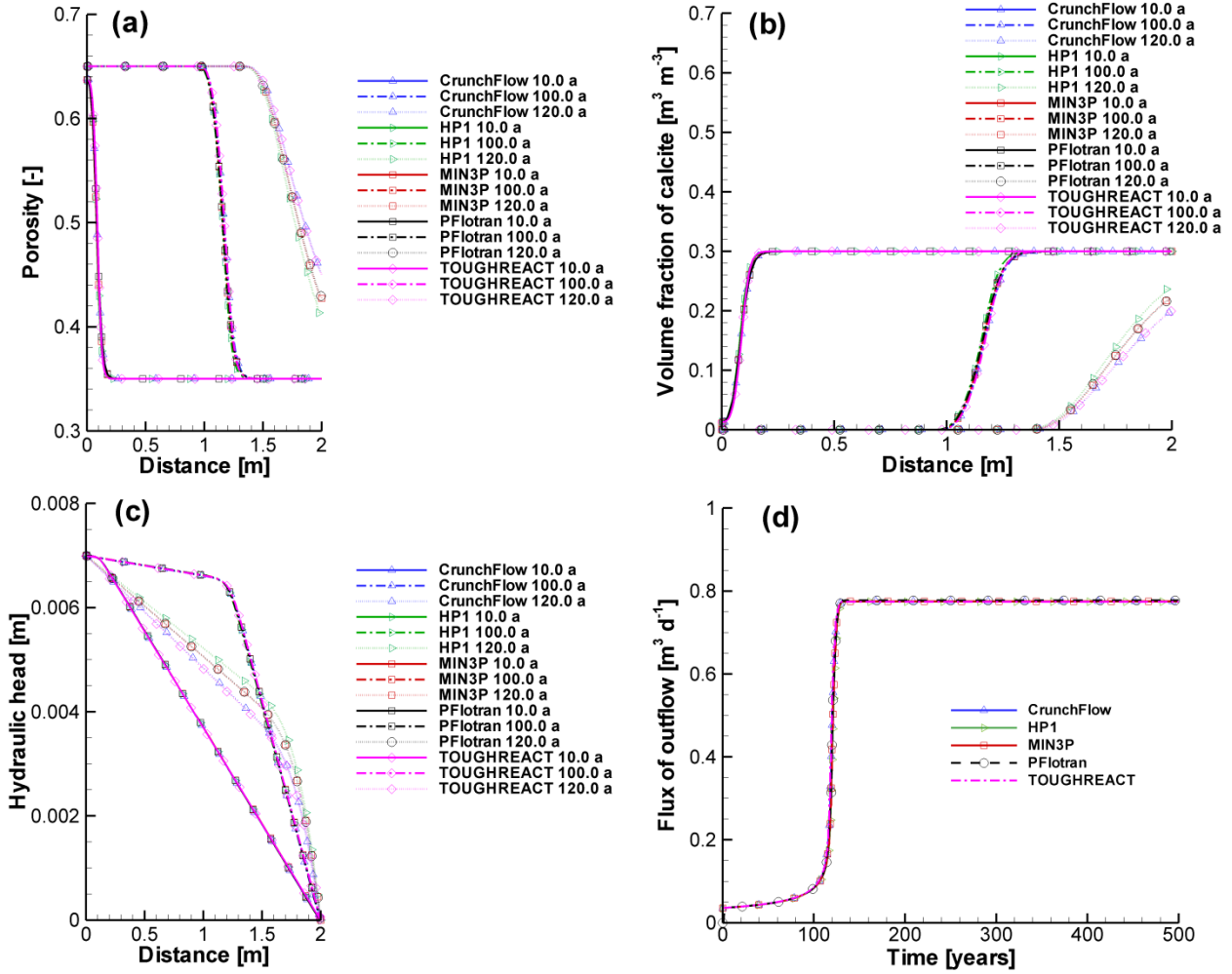**(right)**

475

Figure 2 **Profiles of porosity (a), volume fraction of calcite (b), hydraulic head (c) at 10, 100 and 120 years, and flux time curve (d) from the outflow boundary simulated by CrunchFlow, HP1, MIN3P, PFlotran and TOUGHREACT**
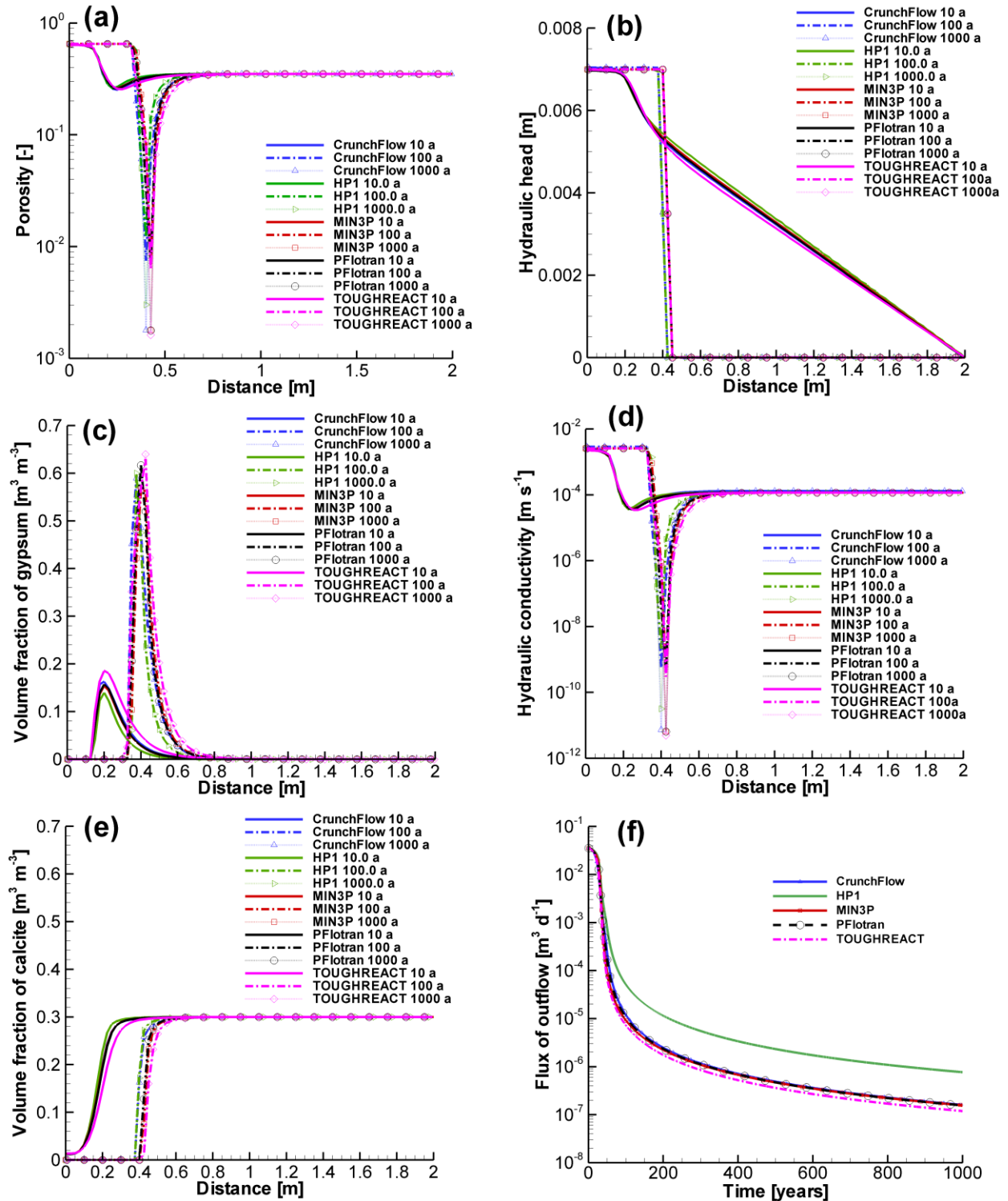
479

28

480

Figure 3 Profiles (B2) of porosity (a), volume fraction of gypsum (c) and calcite (e), hydraulic head (b), hydraulic conductivity (d) at 10, 100 and 120 years, and flux from the outflow boundary (f) simulated by CrunchFlow, HP1, MIN3P, PFlotran and TOUGHREACT
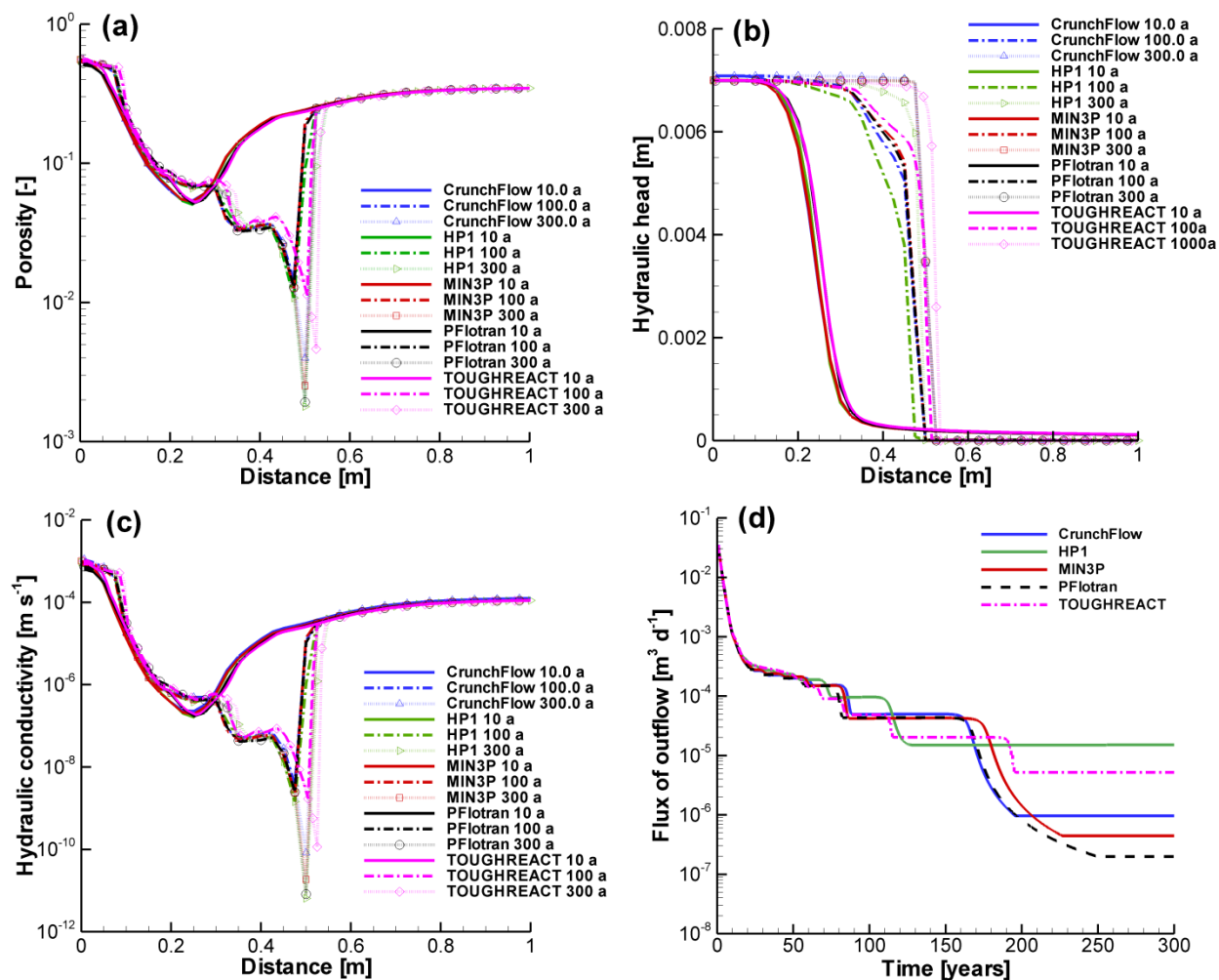
29

485

486

Figure 4   Comparison of profiles (B3) of porosity, hydraulic head and hydraulic conductivity at 10, 100 and 300 years, and outflux time curve from the outflow boundary simulated by CrunchFlow, HP1, MIN3P, PFlotran and TOUGHREACT
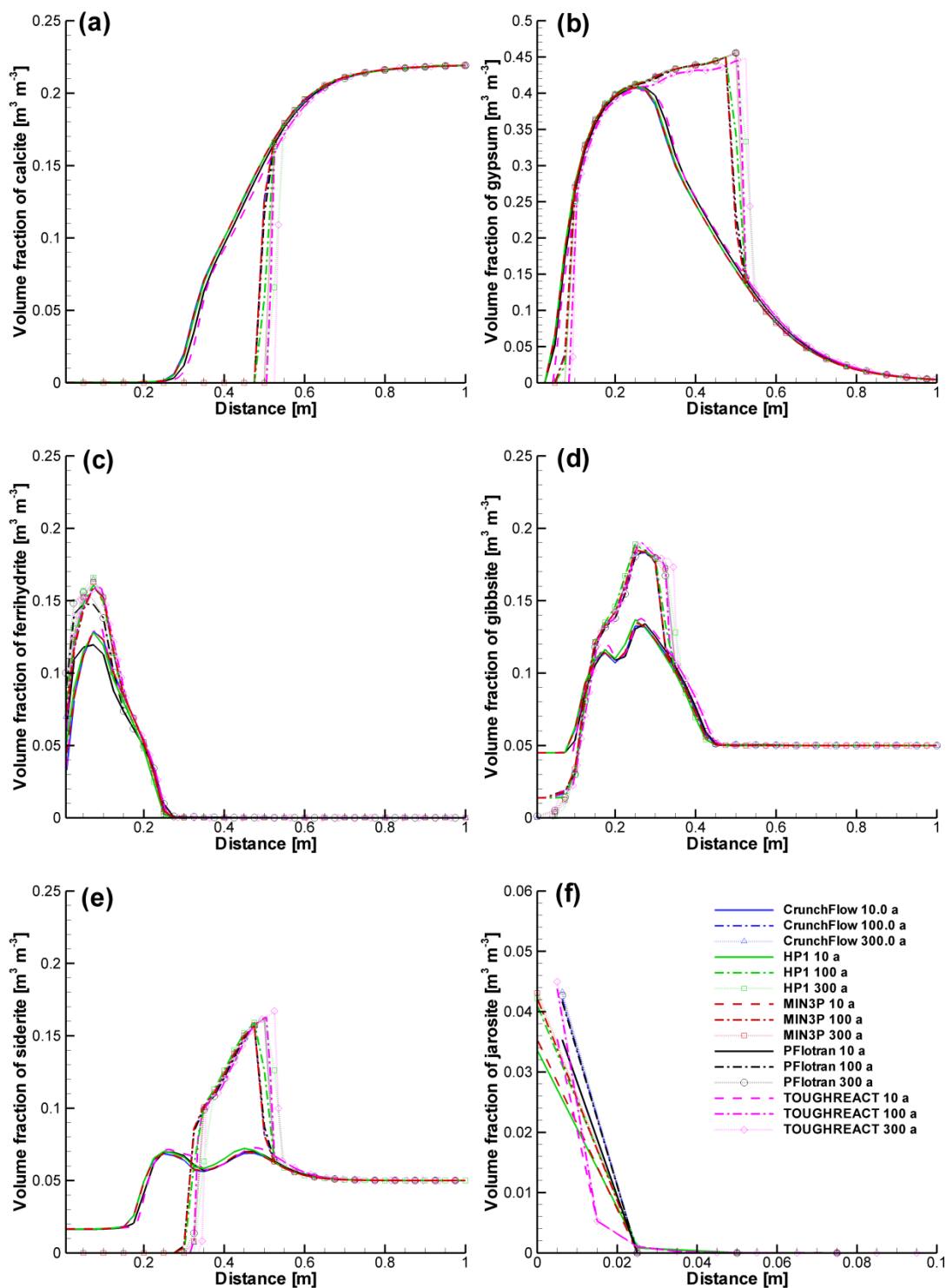
490

30

491

Figure 5   **Comparison of volume fraction profiles (B3) of calcite (a), gypsum (b), ferrihydrite (c), gibbsite (d), siderite (e) and jarosite (f) at 10, 100 and 300 years simulated by CrunchFlow, HP1, MIN3P, PFlotran and TOUGHREACT**
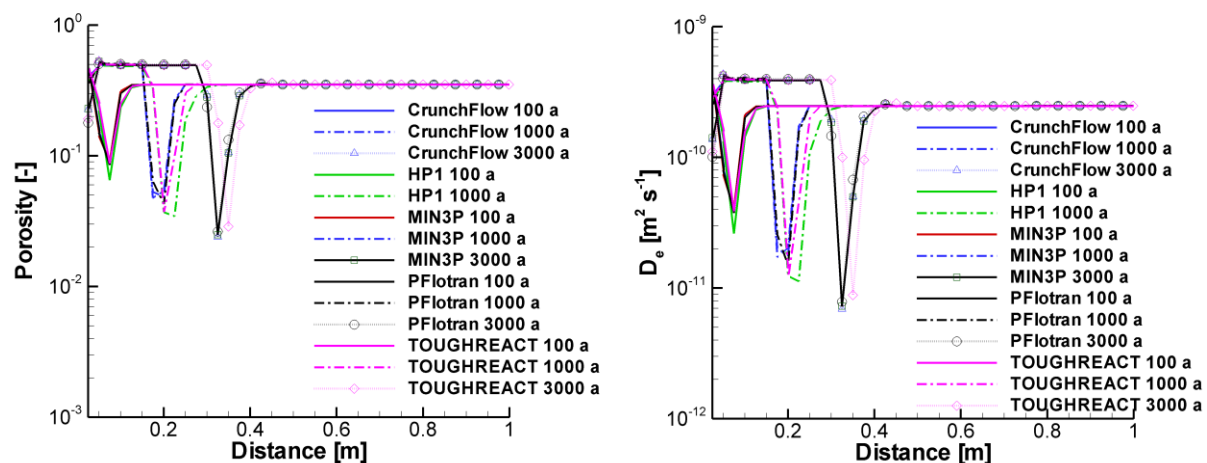
Figure 6   Comparison of profiles (B4) of porosity (left) and effective diffusion coefficient (D_e) (right) at 100, 1000 and 3000 years simulated by CrunchFlow, MIN3P, PFlotran, TOUGHREACT and HP1 (at 100 and 1000 years)
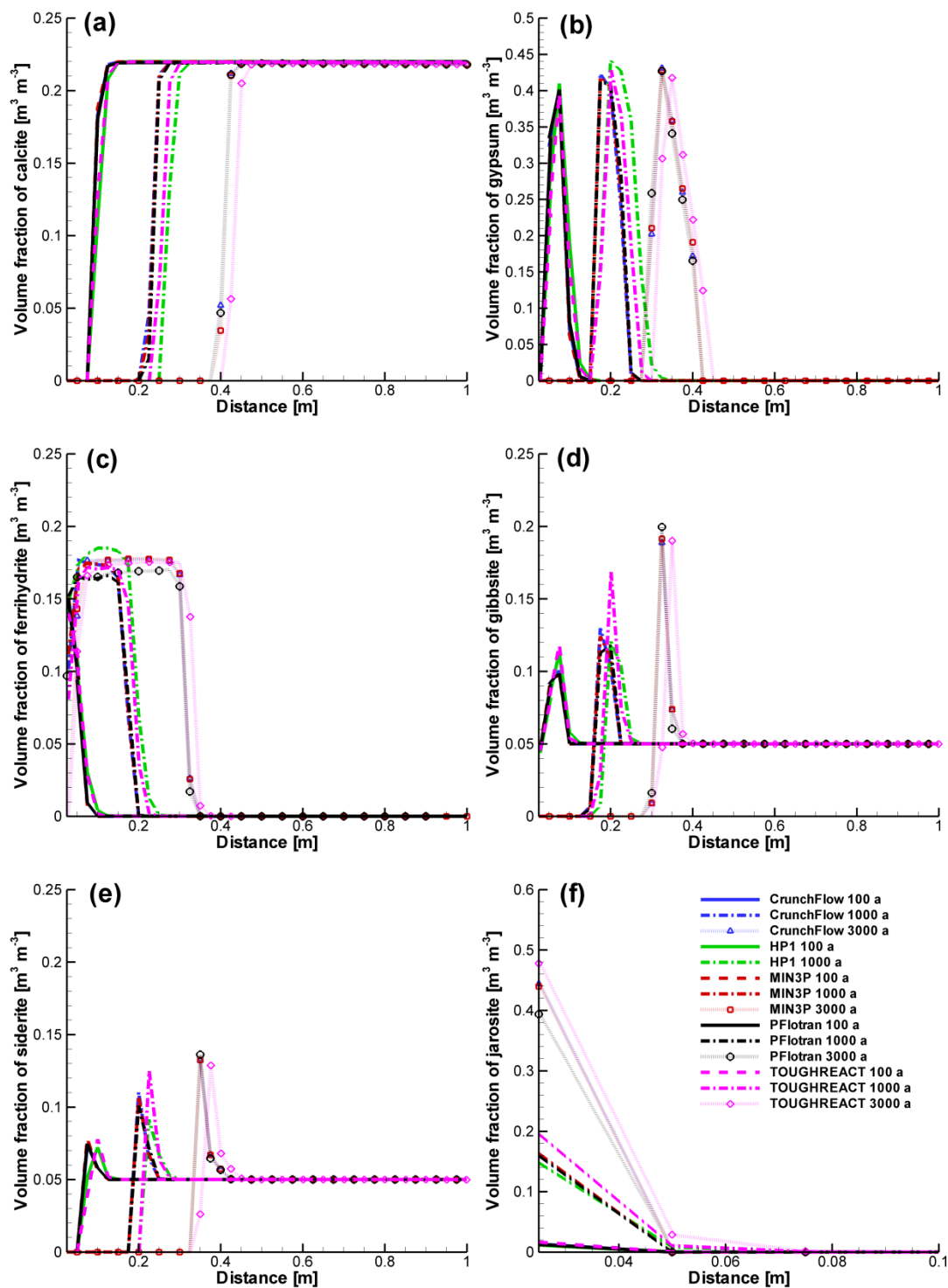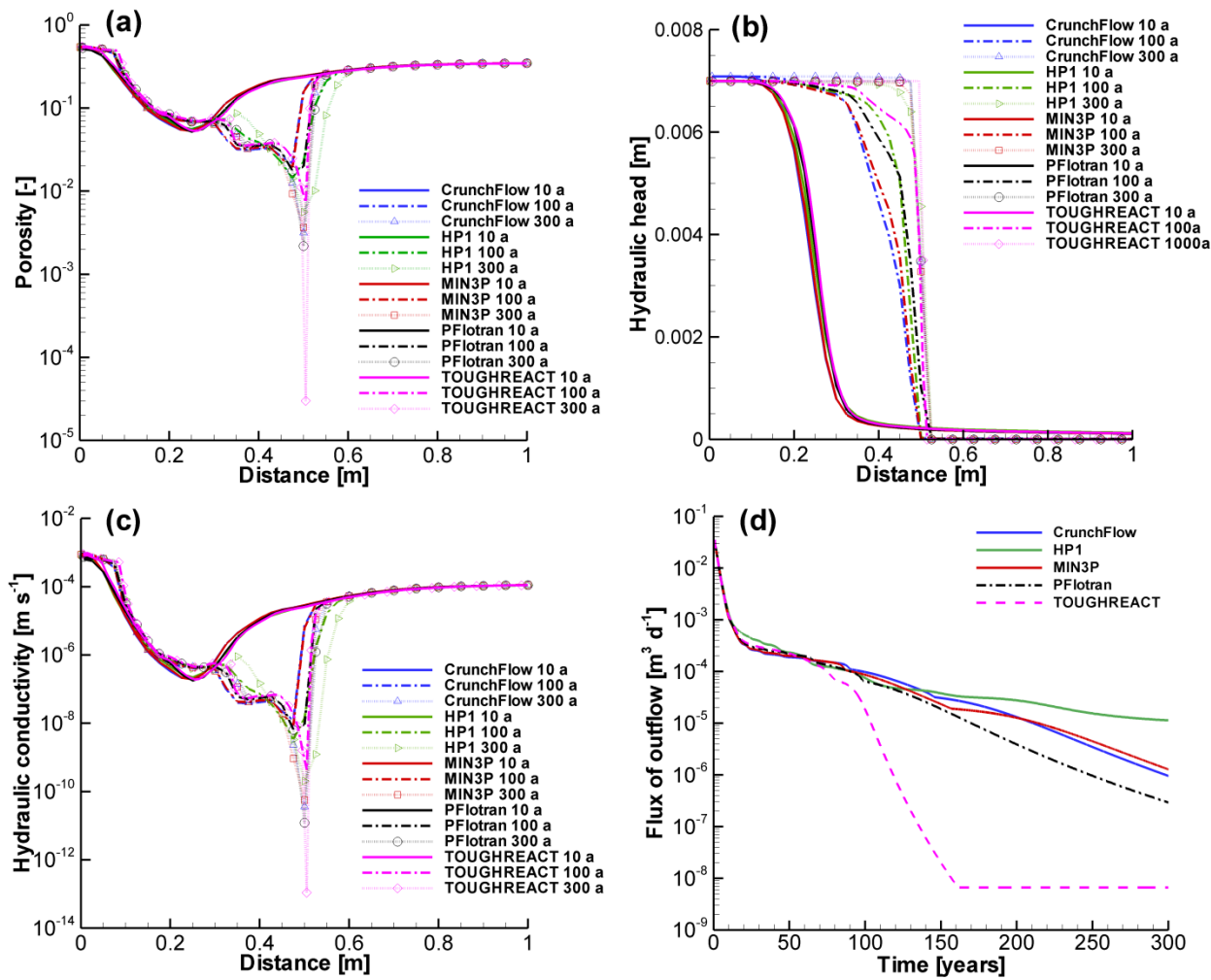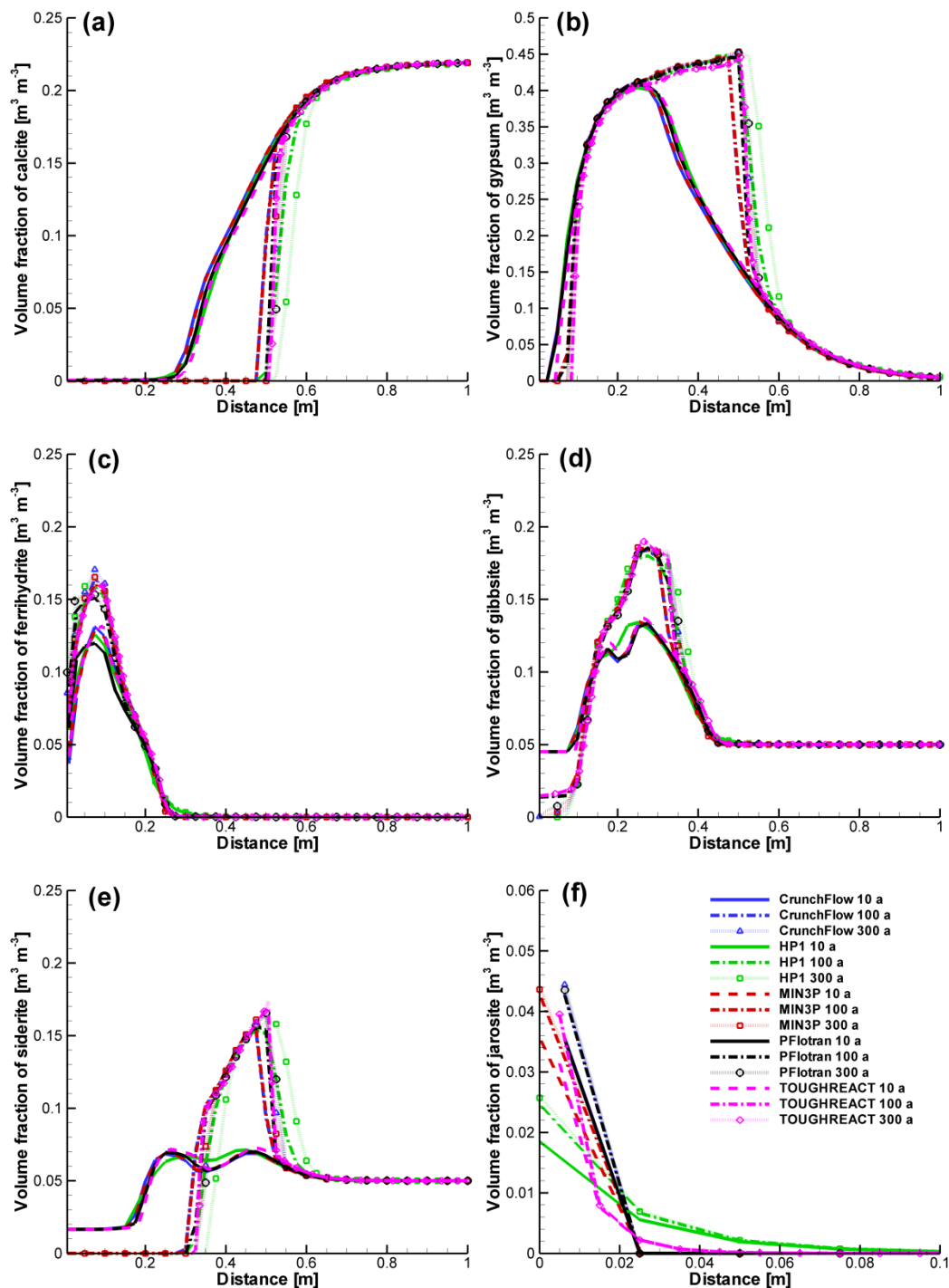
500

Figure 7   **Comparison of mineral volume fraction profiles (B4) of calcite (a), gypsum (b), ferrihydrite (c), gibbsite (d), siderite (e) and jarosite (f) at 100, 1000 and 3000 years simulated by CrunchFlow, MIN3P, PFlotran and TOUGHREACT, and HP1 (for 100 and 1000 years)**

505

506

507

Figure 8   Comparison of profiles (B5) of porosity (a), hydraulic head (b) and hydraulic conductivity (c) at 10, 100 and 300 years, and outflux time curve from the outflow boundary (d) simulated by CrunchFlow, HP1, MIN3P, PFlotran and TOUGHREACT

512

513

Figure 9   Comparison of volume fraction profiles (B5) of calcite (a), gypsum (b), ferrihydrite (c), gibbsite (d), siderite (e) and jarosite (f) at 10, 100 and 300 years simulated by CrunchFlow, HP1, MIN3P, PFlotran and TOUGHREACT

514
515
516
517
518

519
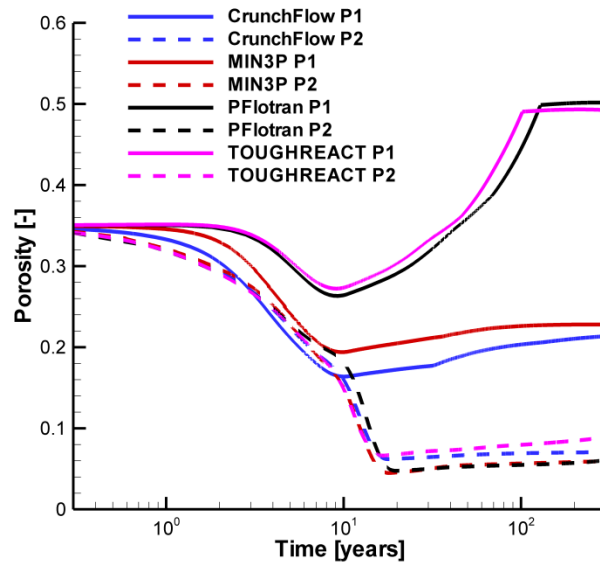
Figure 10 **Comparison of porosity evolution (B6) at observation point P1 (0.1 m, 1.0 m)**
521 **and P2 (0.5 m, 1.0 m) simulated by CrunchFlow, MIN3P, PFlotran and TOUGHREACT**
522

523

524
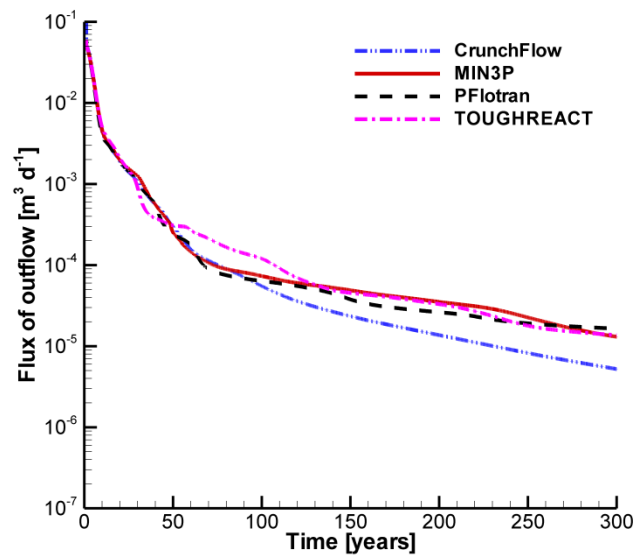
Figure 11   Comparison of flux evolution at outflow boundary (B6) simulated by CrunchFlow, MIN3P, PFlotran and TOUGHREACT

527

528

529

Figure 12   2D distribution of porosity (B6) simulated by MIN3P, CrunchFlow and PFlotran and TOUGHREACT at 300 years, and the positions of the observation points P1 (x = 0.1 m, z = 1.0 m) and P2 (x = 0.5 m, z = 1.0 m)

534   **Supporting Information: Implementation and evaluation of**

535   **permeability-porosity and tortuosity-porosity relationships linked to**

536   **mineral dissolution-precipitation**

537   Mingliang Xie[1,*], K. Ulrich Mayer[1], Francis Claret[2], Peter Alt-Epping[3], Diederik Jacques[4], Carl
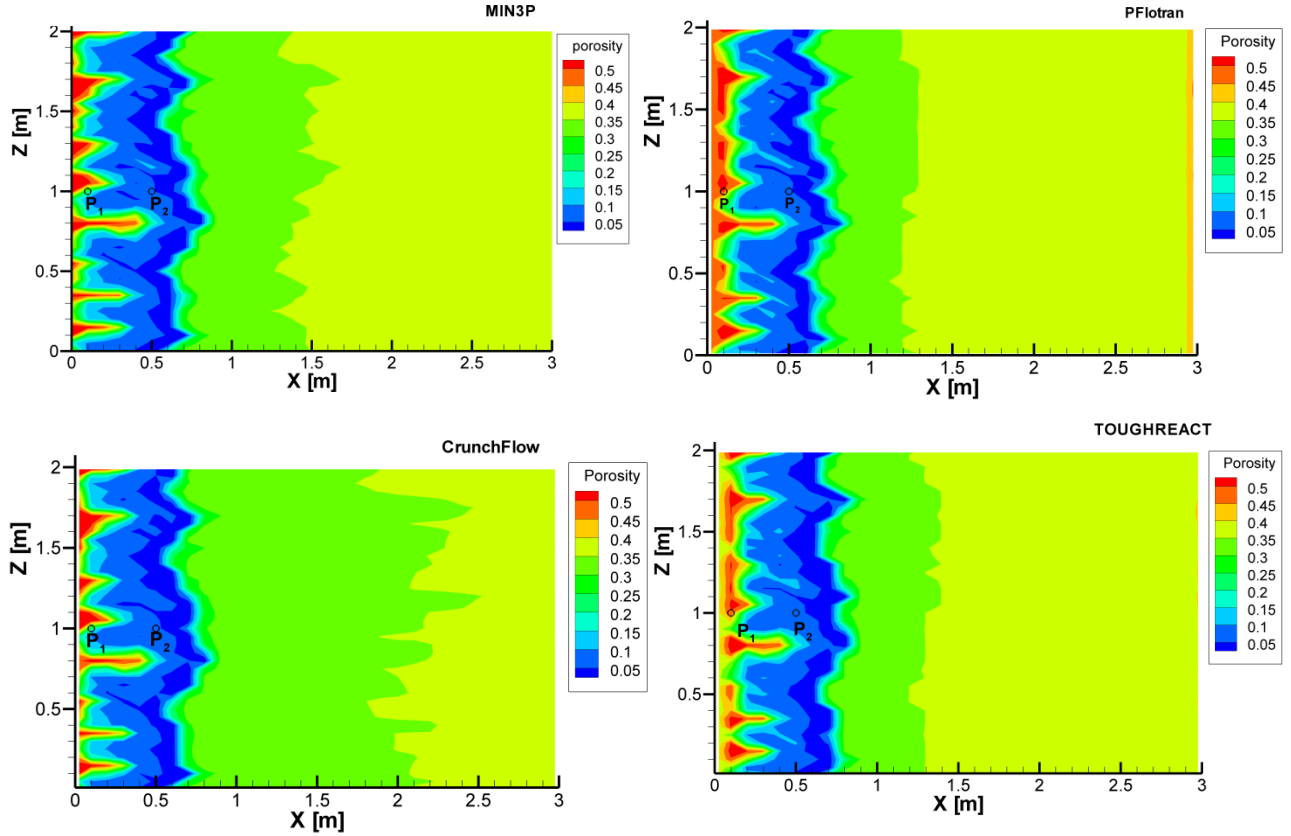538   Steefel[5], Christophe Chiaberge[2] and Jiri Simunek[6]
539
540
541
542   1. Department of Earth, Ocean and Atmospheric Sciences. The University of British Columbia,

543   Vancouver, BC, Canada

544   2. BRGM, 45060 Orleans Cedex, France

545   3. Rock-Water Interaction Group, University of Bern, Institute of Geological Sciences, 3012

546   Bern, Switzerland

547   4. Belgian Nuclear Research Centre SCK.CEN, Mol, Belgium B-2400

548   5. Lawrence Berkeley National Laboratory, Berkeley, CA 94720, USA

549   6. University of California, Riverside, CA 92521, USA

550   * Corresponding author mxie@eos.ubc.ca
551

Table S-1 **Physical and thermodynamic parameters for components**

Component	Charge	Debye-Huckel constants		Molar weight [g mol^{-1}]	Alkalinity factor
		a	b		
$O_2(aq)$	0.0	3.0	0	31.9998	0
H_2O	0.0	0.0	0	18.0153	0
Al^{+3}	3.0	9.0	0	26.9815	0
CO_3^{-2}	-2.0	5.4	0	60.0094	2
Ca^{+2}	2.0	6.0	0.17	40.08	0
Fe^{+2}	2.0	6.0	0	55.847	0
Fe^{+3}	3.0	9.0	0	55.847	0
H^+	1.0	9.0	0	1.008	-1
K^+	1.0	3.0	0.01	39.102	0
Na^+	1.0	4.0	0.07	22.9898	0
SO_4^{-2}	-2.0	4.0	-0.04	96.0616	0

553
554
555

Table S-2   Geochemical reactions of aqueous species and thermodynamic parameters

Species	Mol mass [g mol^{-1}]	Reaction	logK$_{25}$	Debye Hueckel constant	
				a	b
KHSO$_4$(aq)	136.1716	KHSO$_4$(aq) = K$^+$ + H$^+$ + SO$_4^{2-}$	0.8136	0.00	0.00
H$_2$SO$_4$(aq)	98.0776	2H$^+$ + SO$_4^{2-}$ = H$_2$SO$_4$(aq)	-1.0209	0.00	0.00
H$_2$(aq)	2.0160	H$_2$O – 0.5 O$_2$(aq) = H$_2$(aq)	-46.1070	0.00	0.00
FeCO$_3^+$	115.8562	Fe^{3+} +CO$_3^{2-}$ = FeCO$_3^+$	9.7200	0.00	0.00
OH$^-$	17.0074	H$_2$O-H+ = OH$^-$	-13.9980	3.50	0.00
CaOH$^+$	57.0870	Ca^{2+} + H$_2$O – H$^+$ = CaOH$^-$	-12.7800	6.00	0.00
CaHCO$_3^+$	101.0970	Ca^{2+} + CO$_3^{2-}$ + H$^+$ = CaHCO$_3^+$	11.4400	6.00	0.00
CaCO$_3$aq	100.0890	Ca^{2+} + CO$_3^{2-}$ = CaCO$_3$(aq)	3.2200	0.00	0.00
CaSO$_4$aq	136.1410	Ca^{2+} + SO$_4^{2-}$ = CaSO$_4$(aq)	2.3090	0.00	0.00
CaHSO$_4^+$	137.1489	Ca^{2+} + SO$_4^{2-}$ + H$^+$ = CaHSO$_4^+$	3.0680	0.00	0.00
NaCO$_3^-$	82.9990	Na$^+$ + CO$_3^{2-}$ = NaCO$_3^-$	1.2680	5.40	0.00
NaHCO$_3$aq	84.0070	Na$^+$ + CO$_3^{2-}$ + H$^+$ = NaHCO$_3$(aq)	10.0800	0.00	0.00
NaSO$_4^-$	119.0510	Na$^+$ + SO$_4^{2-}$ = NaSO$_4^-$	0.7000	5.40	0.00
KSO$_4^-$	135.163	K$^+$ + SO$_4^{2-}$ = KSO$_4^-$	0.8500	5.40	0.00
AlOH^{2+}	43.988	Al^{3+} + H$_2$O – H$^+$ = AlOH^{2+}	-4.9900	5.40	0.00
Al(OH)$_2^+$	60.996	Al^{3+} 2+ H$_2$O – 2 H$^+$ = Al(OH)$_2^+$	-10.1000	5.40	0.00
Al(OH)$_4^-$	95.011	Al^{3+} +4 H$_2$O – 4 H$^+$ = Al(OH)$_4^-$	-22.7000	4.50	0.00
AlSO$_4^+$	123.043	Al^{3+} + SO$_4^{2-}$ = AlSO$_4^+$	3.5000	4.50	0.00
AlHSO$_4^{2+}$	124.0509	Al^{3+} + SO$_4^{2-}$ + H$^+$ = AlHSO$_4^{2+}$	2.4480	4.50	0.00
Al(SO$_4$)$_2$-	219.104	Al^{3+} + 2 SO$_4$2- = Al(SO$_4$)$_2^-$	5.0000	4.50	0.00
Al(OH)$_3$aq	78.003	Al^{3+} 3+ H$_2$O – 3 H$^+$ = Al(OH)$_3$(aq)	-16.9000	0.00	0.00
FeOH$^+$	72.854	Fe^{2+} + H$_2$O – H$^+$ = FeOH$^+$	-9.5000	5.00	0.00
Fe(OH)$_3^-$	106.869	Fe^{2+} + 3 H$_2$O – 3 H$^+$ = Fe(OH)$_3^-$	-31.0000	5.00	0.00
FeSO$_4$aq	151.908	Fe^{2+} + SO$_4^{2-}$ = FeSO$_4$(aq)	2.2500	0.00	0.00
FeHSO$_4^+$	152.9159	Fe^{2+} + SO$_4^{2-}$ + H$^+$ = FeHSO$_4^+$	3.0680	0.00	0.00
FehCO$_3^+$	116.8641	Fe^{2+} + CO$_3^{2-}$ + H$^+$ = FeHCO$_3^+$	12.3300	0.00	0.00
FeCO$_3$aq	115.8562	Fe^{2+} + CO$_3^{2-}$ = FeCO$_3$aq	4.3800	0.00	0.00
Fe(OH)$_2$aq	89.861	Fe^{2+} + 2 H$_2$O – 2 H$^+$ = Fe(OH)$_2$(aq)	-20.5700	0.00	0.00
FeOH^{2+}	72.854	Fe^{3+} + H$_2$O – H$^+$ = FeOH^{2+}	-2.1900	5.00	0.00
FeSO$_4^+$	151.908	Fe^{3+} + SO$_4^{2-}$ = FeSO$_4^+$	4.0400	5.00	0.00
FeHSO$_4^{2+}$	152.9079	Fe^{3+} + SO$_4^{2-}$ + H$^+$ = FeHSO$_4^{2+}$	4.4780	5.00	0.00
Fe(OH)$_2^+$	89.861	Fe^{3+} + 2 H$_2$O – 2 H$^+$ = Fe(OH)$_2^+$	-5.6700	5.40	0.00
Fe(OH)$_3$aq	106.869	Fe^{3+} + 3 H$_2$O – 3 H$^+$ = Fe(OH)$_3$(aq)	-12.5600	0.00	0.00
Fe(OH)$_4^-$	123.876	Fe^{3+} + 4 H$_2$O – 4 H$^+$ = Fe(OH)$_4^-$	-21.6000	5.40	0.00
Fe(SO$_4$)$_2^-$	247.97	Fe^{3+} + 2SO$_4^{2-}$ = Fe(SO$_4$)$_2^-$	5.3800	0.00	0.00
Fe$_2$(OH)$_2^{+4}$	145.708	2 Fe^{3+} + 2 H$_2$O – 2 H$^+$ = Fe$_2$(OH)$_2^{+4}$	-2.9500	0.00	0.00
Fe$_3$(OH)$_4^{+5}$	235.57	3 Fe^{3+} +4 H$_2$O -4 H$^+$ = Fe$_3$(OH)$_4^{+5}$	-6.3000	0.00	0.00
HCO$_3^-$	61.0170	H$^+$ + CO$_3^{2-}$=HCO$_3^-$	10.3300	5.40	0.00
H$_2$CO$_3$aq	62.0250	2H$^+$ + CO$_3^{2-}$=H$_2$CO$_3$(aq)	16.6810	0.00	0.00
HSO$_4^-$	97.0690	SO$_4^{2-}$ + H$^+$= HSO$_4^+$	1.9870	4.50	0.00

558

559 The following equilibrium redox reaction is considered for the benchmarks B3 - B6:

560

561 $Fe^{3+} \leftrightarrow Fe^{2+} + ¼ O_2(aq) + H^+ - ½ H_2O$ $\log K_{25} = -8.4725$

562

563
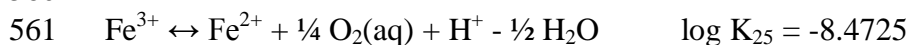
Reference model results produced by MIN3P were included in EXCEL files:

565 Figure 2: Xie-et-al-2014-B1-Fig2.xlsx

566 Figure 3: Xie-et-al-2014-B2-Fig3.xlsx

567 Figure 4: Xie-et-al-2014-B3-Fig4.xlsx

568 Figure 5: Xie-et-al-2014-B3-Fig5.xlsx

569 Figure 6: Xie-et-al-2014-B4-Fig6.xlsx

570 Figure 7: Xie-et-al-2014-B4-Fig7.xlsx

571 Figure 8: Xie-et-al-2014-B5-Fig8.xlsx

572 Figure 9: Xie-et-al-2014-B5-Fig9.xlsx

573 Figure 10: Xie-et-al-2014-B6-Fig10.xlsx

574 Figure 11: Xie-et-al-2014-B6-Fig11.xlsx

575 Figure 12: Xie-et-al-2014-B6-Fig12.xlsx

Compressed File

[Click here to download Compressed File: SupportingInformationPartII.zip](#)